



HAL
open science

Electron Density and Optoelectronic Properties of Copper Antimony Sulphur Ternary Compounds for Photovoltaic Applications

Mohamed Khairy, Pingping Jiang, Pascal Boulet, Marie-Christine Record

► **To cite this version:**

Mohamed Khairy, Pingping Jiang, Pascal Boulet, Marie-Christine Record. Electron Density and Optoelectronic Properties of Copper Antimony Sulphur Ternary Compounds for Photovoltaic Applications. *Journal of Electronic Materials*, 2022, 51 (7), pp.3903-3918. 10.1007/s11664-022-09650-3 . hal-03983411

HAL Id: hal-03983411

<https://amu.hal.science/hal-03983411>

Submitted on 27 Mar 2023

HAL is a multi-disciplinary open access archive for the deposit and dissemination of scientific research documents, whether they are published or not. The documents may come from teaching and research institutions in France or abroad, or from public or private research centers.

L'archive ouverte pluridisciplinaire **HAL**, est destinée au dépôt et à la diffusion de documents scientifiques de niveau recherche, publiés ou non, émanant des établissements d'enseignement et de recherche français ou étrangers, des laboratoires publics ou privés.

Electron Density and Optoelectronic Properties of Copper-Antimony-Sulphur Ternary Compounds for Photovoltaic Applications

Mohamed Khairy¹, Pingping Jiang^{2,3,4}, Pascal Boulet² and Marie-Christine Record^{3,*}

¹ Chemistry Department, Faculty of Science, Sohag University, 82524;

² Aix-Marseille University, CNRS, MADIREL, F-13013 Marseille, France;

³ Aix-Marseille University, University of Toulon, CNRS, IM2NP, F-13013 Marseille, France ;

⁴ Current address: Univ Rennes, INSA Rennes, CNRS, Institut FOTON - UMR 6082, F-35000 Rennes

*Corresponding author: m-c.record@univ-amu.fr

Abstract: Design of efficient solar energy-conversion materials has attracted much interest in the last decades. Among these materials, copper-based semiconducting chalcogenides have been employed as alternatives for copper indium gallium selenide (CIGS) thin-film solar cells due to their low toxicity and earth-abundant absorber components. In the present manuscript, structural, electronic, topological, and optical properties of ternary chalcogenide CuSbS_2 , Cu_3SbS_3 , and Cu_3SbS_4 have been investigated using the full potential linear augmented plane wave (FP-LAPW) method. An indirect bandgap is observed for CuSbS_2 with $E_g = 1.178$ eV and a direct bandgap is found for Cu_3SbS_3 , and Cu_3SbS_4 with $E_g = 1.283$ and 1.0 eV, respectively. The valence band maximum (VBM) of CuSbS_2 , Cu_3SbS_3 , and Cu_3SbS_4 are mainly predominated by a strong Cu-3d and S-3p orbitals hybridization. The conduction band of CuSbS_2 and Cu_3SbS_3 are mainly characterized by Sb-5p orbital and S-3p orbital mixing. However, conduction band of Cu_3SbS_4 is dominated by the mixing of Sb-5s and S-3p orbitals. It is found that the Cu-S and Sb-S bonds lie in the transit closed-shell zone, between the typical ionic and covalent bonds. The optical properties of CuSbS_2 , Cu_3SbS_3 , and Cu_3SbS_4 in terms of absorption coefficient, extinction coefficient, refractive index, and reflectivity have been investigated. The results show that the CuSbS_2 , Cu_3SbS_3 , and Cu_3SbS_4 compounds have real potential to be used for solar-energy conversion.

Keywords: Copper-based chalcogenides; DFT; optoelectronic properties; electron density topology; solar-energy conversion

1. Introduction

The search for and design of efficient solar energy-conversion materials have attracted much interest in the last decades in order to overcome the global energy shortage and CO₂ emission in the inevitable future expansion [1]. In 2019, the producing capacity of solar photovoltaic (PV) reached about 633 GW, with a 24 % growth year-on-year, and might foresee reaching 4.7 terawatts by 2050 as proposed by the International Energy Agency (IEA). More than 90% of world production capacity is held by crystalline silicon modules, which are being very effective. The cheaper thin-film compound semiconductors might be alternatives and strong competitors to silicon PV. Recently, transition metal chalcogenides have enabled a breakthrough in the development of thin-film photovoltaic solar cells because of their optoelectronic properties in terms of photo-stability and high-surface-area visible-light absorber [2]. For example, the copper indium gallium selenide (CIGS) and cadmium telluride (CdTe) solar cells revealed a spectroscopic limited maximum efficiency (SLME) of about 20.8% and 19.6%, respectively. Although these thin-film photovoltaic cells are commercially available, their elemental components are toxic and relatively rare, which limits their terawatt scale productions [3]. The copper-zinc tin sulfoselenide (CZTSSe) was explored as a promising alternative material because it might fulfill the prerequisites for sufficient solar irradiation but still, the efficiency of PV devices is relatively low, despite more than a decade of painstaking researches [4]. The copper-based chalcogenide systems including CuSbS₂ (Chalcostibite), Cu₃SbS₄ (Famatinite), Cu₁₂Sb₄S₁₃ (Tetrahedrite), and Cu₃SbS₃ (Skinnerite) phases have been explored as they are interesting alternatives for CIGS thin-film solar cells due to their low-toxicity and earth-abundant absorber components [3,5-13]. The Cu-Sb-S system compounds are p-type semiconductors with optical band gap (E_g) ranging between 0.5 and 2.0 eV and a large absorption coefficient over 10^4 cm^{-1} at visible wavelengths, which shows a comparable efficiency (i.e., 22.9%) to that of CIGS and CZTSSe [14]. Yet, due to a lack of knowledge in the fundamental physical properties comprehension these compounds have not reached the stage of being integrated into devices. Therefore, further developments in PV technology based on these compounds call for a deep understanding of the electronic and optical properties of these materials and of their structure-properties relationships, which is the topic of the present work.

In this work, we have investigated the structural, electronic, and optical properties of ternary chalcogenide CuSbS₂, Cu₃SbS₃, and Cu₃SbS₄ using density functional theory (DFT) calculations with the full-potential linearized augmented plane-wave (FP-LAPW) method that was suggested to be one of the most efficient methods to solve many-electron problems in the solid crystal. In order to try to understand the relationship between bond interactions and optoelectronic properties, the electron density topology has been investigated as

well using Bader's quantum theory of atoms in molecules (QTAIM) [15]. $\text{Cu}_{12}\text{Sb}_4\text{S}_{13}$ has not been considered in the present work as it shows a semi-metallic behaviour [3]. The investigation of the structure-properties relationship in the Cu-Sb-S compounds has never been done to date. Although the optical properties have already been published for CuSbS_2 [3,17-18], Cu_3SbS_3 [3] and Cu_3SbS_4 [3,19], we have re-investigated these properties for the three compounds with the same procedure, as our aim is to study the relation between the electronic densities and the optical properties.

2. Computational details

First principle density functional theory calculations using the FP-LAPW method based on Kohn-Sham equations have been carried out using the WIEN2k package [20]. The structural optimizations have been performed using the generalized gradient approximation (GGA) with the Perdew, Burke, and Ernzerhof (PBE) functionals [21] as implemented in the WIEN2k package. As the modified Becke-Johnson (mBJ) potential allows for estimating bandgap energies more accurately it has been used to calculate electron band structures and density of states [22-24]. Unfortunately, since the mBJ functional gave wrong bandgap energy for Cu_3SbS_4 , the hybrid functional of Heyd, Scuseria, and Ernzerhof (HSE06) has been utilized for this compound [25]. The core-valence electron separation has been defined as follows: Cu [Ar] $3d^{10} 4s^1$, Sb [Kr] $4d^{10} 5s^2 5p^3$, and S [Ne] $3s^2 4p^4$. The structure optimization has been performed by calculating the total energy (in Ry) with respect to crystal volume, b/a, and c/a ratio in proper sequence and full structure relaxation has been carried out until the total residual forces on all atoms were less than 2 mRy per Bohr. The optimized volumes and cell parameters have been obtained from fitting curves against the Birch-Murnaghan equation of state:

$$E(V) = E_o + \left(\frac{9V_o}{16}\right)\left(\frac{B}{4703.6}\right)(\eta^2 - 1)^3 B_p + (\eta^2 - 1)^2 (6 - 4\eta^2), \quad (1)$$

$$\eta = \left(\frac{V_o}{V}\right)^{\frac{1}{3}}, \quad (2)$$

where, V_o , and V are the initial and distorted volumes, B is the bulk modulus, and B_p is the derivative of bulk modulus with respect to pressure.

The convergence parameter $R_{\text{MT}}K_{\text{max}}$ has been set to 7, where R_{mt} is the radius of the smallest sphere and K_{max} is a maximum wave vector. The charge density has been obtained up to $G_{\text{max}}=14$ (a.u.)⁻¹. For the mBJ calculations, the Brillouin zone has been sampled with a mesh of 1000 k-points. For hybrid calculations, a $6 \times 6 \times 6$ grid of 30 k-points has been used. A $16 \times 16 \times 16$ k-points grid (4096 k-points in the full Brillouin zone) has been used for optical calculations.

The optical properties of the Cu-Sb-S compounds have been calculated based on their response to electromagnetic perturbations as implemented in Wien2k [26]. The frequency-dependent complex dielectric function has been determined as $\varepsilon(\omega) = \varepsilon_1(\omega) + i\varepsilon_2(\omega)$, where ω is the photon frequency. The imaginary (absorptive) part of dielectric function $\varepsilon_2(\omega)$ is calculated using the following momentum matrix elements between the valence and conduction wave functions:

$$\varepsilon_2(\omega) = \frac{e^2 \hbar}{\pi m^2 \omega^2} \sum_{v,c} \int_{BZ} |M_{cv}(\mathbf{k})|^2 \delta\{\omega_{cv}(\mathbf{k}) - \omega\} d^3 \mathbf{k}. \quad (3)$$

The real (dispersive) part of the dielectric function $\varepsilon_1(\omega)$ and the absorption coefficient $\alpha(\omega)$ have been calculated by Kramers–Kronig transformation as:

$$\varepsilon_1(\omega) = 1 + \frac{2}{\pi} P \int_0^{\infty} \frac{\omega' \varepsilon_2(\omega')}{\omega'^2 - \omega^2} d\omega', \quad (4)$$

$$\alpha(\omega) = \sqrt{2} \omega \left[\sqrt{\varepsilon_1(\omega)^2 + \varepsilon_2(\omega)^2} - \varepsilon_1(\omega) \right]^{\frac{1}{2}}, \quad (5)$$

where P is the momentum operator. The extinction coefficient $k(\omega)$, energy loss $L(\omega)$, and refractive index $n(\omega)$ have been calculated using real and imaginary parts of dielectric function as:

$$k(\omega) = \left[\frac{\sqrt{\varepsilon_1^2(\omega) + \varepsilon_2^2(\omega)}}{2} - \frac{\varepsilon_1(\omega)}{2} \right]^{\frac{1}{2}}, \quad (6)$$

$$L(\omega) = \frac{\varepsilon_2(\omega)}{\varepsilon_1(\omega)^2 + \varepsilon_2(\omega)^2}, \quad (7)$$

$$n(\omega) = \left[\frac{\varepsilon_1(\omega)}{2} + \frac{\sqrt{\varepsilon_1^2(\omega) + \varepsilon_2^2(\omega)}}{2} \right]^{\frac{1}{2}}, \quad (8)$$

The reflectivity has been calculated by the following equation:

$$R(\omega) = \frac{(n(\omega)-1)^2 + k(\omega)^2}{(n(\omega)+1)^2 + k(\omega)^2}. \quad (9)$$

The real-space analysis of the quantum chemical interactions has been carried out using Critic2 program [27].

3. Results and discussion

3.1. Crystal structures of the Cu-Sb-S system compounds

The crystal structure of $\text{Cu}^{\text{I}}\text{Sb}^{\text{III}}\text{S}^{\text{II}}$ (CuSbS_2 , Chalcostibite) is composed of square pyramidal SbS_5 units, which share their edges to form continuous SbS_2 units aligned with the b axis. The SbS_2 units are regularly separated by CuS_4 tetrahedra. Thus, the bases of the square pyramidal units are lined up to face one another and the Sb electron lone pair points towards the void separating the SbS_5 units (Fig. 1a). The $\text{Cu}^{\text{I}}\text{Sb}^{\text{III}}\text{S}^{\text{II}}$ (Cu_3SbS_3) has a

Skinnerite structure and derives from the Wittichenite structure. The Cu atoms are in nearly trigonal planar coordination with S atoms, the Sb atom is trigonally coordinated by S, and S is tetrahedrally coordinated by three Cu atoms and one Sb atom. As can be seen in Figure 1b, there are different crystallographic positions for both Cu and Sb atoms. The crystal structure of $\text{Cu}^{\text{I}}\text{Sb}^{\text{V}}\text{S}_4$ (Famatinite) derives from the zinc blende structure, which is characterized by S atoms laying at the nodes of a face-centred cubic lattice and Cu or Sb atoms located in the tetrahedral sites and forming MS_4 units. The Cu atoms are classified as Cu1 and Cu2, which occupy Wyckoff 2b and 4d positions, while Sb and S atoms occupy 2a and 8i ones, respectively (Fig. 1c). Thus, two types of Cu–S bond and one type of Sb–S bond can be distinguished. Table I gathers the lattice constants calculated in this work with the PBE functional for CuSbS_2 , Cu_3SbS_3 , and Cu_3SbS_4 together with the experimental ones reported in the literature. There is a slight overestimation of the lattice parameters ($< 2\%$) for CuSbS_2 and Cu_3SbS_3 compounds, which is quite reasonable for structural results. Further, the Cu_3SbS_4 structure has been optimized with the HSE06 hybrid functional, which leads to better agreement with experimental cell parameters than the PBE functional.

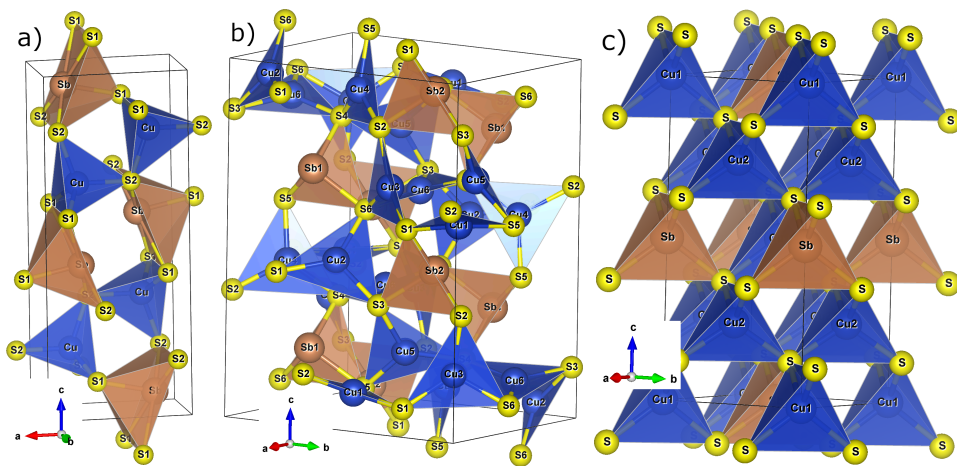


Fig. 1. Optimized crystal of Cu-Sb-S structures. (a) CuSbS_2 , (b) Cu_3SbS_3 and (c) Cu_3SbS_4 .

Table I. Calculated lattice constants compared with experimental literature data.

Compound	Crystal structure	Space group	Lattice constants						Method	Ref.
			a (pm)	b (pm)	c (pm)	α (°)	β (°)	γ (°)		
CuSbS ₂ chalcostibite	Orthorhombic	Pnma (62)	611.8	385.3	1457.3	90	90	90	PBE	This work
	Orthorhombic	Pnma (62)	602.4	378.6	1470.1	90	90	90	Exp.	[2]
	Orthorhombic	Pnma (62)	601.6	379.7	1449.9	90	90	90	Exp.	[28]
	Orthorhombic	Pnma (62)	602.0	379.0	1449.0	90	90	90	Exp.	[29]
Cu ₃ SbS ₃ skinnerite	monoclinic	P121/c (14)	804.5	1034.1	1340.1	90	90.4	90	PBE	This work
	monoclinic	P121/c (14)	780.8	1023.3	1326.8	90	90.4	90	Exp.	[29]
	monoclinic	P121/c (14)	784.6	1024.7	1325.3	90	90.4	90	Exp.	[30]
Cu ₃ SbS ₄ famatinite	Tetragonal	I-42m (121)	549.2	549.2	1085.7	90	90	90	PBE	This work
		I-42m (121)	544.7	544.7	1081.7	90	90	90	HSE06	This work
	Tetragonal	I-42m (121)	539.1	539.1	1087.0	90	90	90	Exp.	[31]
	Tetragonal	I-42m (121)	539.0	539.0	1075.0	90	90	90	Exp.	[32]

3.2 Band structure of Cu-Sb-S system compounds

To understand the electronic properties of the Cu-Sb-S compounds, the band structures and the density of states (DOS) have been calculated using the PBE and mBJ functionals, as well as the HSE06 functional in the particular case of the Cu₃SbS₄ compound. At first, the band structures of CuSbS₂, Cu₃SbS₃, and Cu₃SbS₄ have been calculated with the PBE functional along the high symmetry directions in the Brillouin zone (BZ) (Fig. S1). As the modified mBJ potential allows for estimating bandgap energies more accurately, the band structures of the Cu-Sb-S compounds have been estimated with this potential, the results of which are illustrated in Fig. 2 and Fig. S2. However, the mBJ functional fails to estimate properly the band structure of Cu₃SbS₄ compound (wrong bandgap). Thus, the HSE06 functional has been used (Fig. 2c). The dashed horizontal line represents the position of the Fermi energy level (E_F). The values of the band gaps E_g have been estimated from the energy difference between the conduction band minimum (CBM) and the valence band maximum (VBM) and the data are gathered in Table II. It is found that the value of band gaps calculated using PBE is underestimated in

comparison with experimental values. Furthermore, a closed energy gap calculated with PBE and mBJ around the Fermi level is observed for Cu_3SbS_4 indicating semi-metallic behaviour. With the mBJ potential, the band structure of CuSbS_2 shows a VBM located at the Γ -point and a CBM located between the R and X points. An indirect bandgap of 1.178 eV is then observed, which agrees with the indirect band gap values experimentally reported (Table II). Interestingly, the difference between the lowest direct bandgap and fundamental indirect bandgap is about 0.1 eV, thus, a strong optical absorption might occur at such energy [33]. The band structure of Cu_3SbS_3 shows that the valence band bears two maxima located at the Γ -point and X-point and that the conduction band bears two minima located at the Γ -point and X-point, too. A direct bandgap is observed with a value of 1.283 eV, which is 0.12 eV to 0.59 eV lower than the experimental values (Table II). Furthermore, a flat conduction band bottom is observed. Thus, a strong optical absorption is expected in the Cu_3SbS_3 compound. The band structure of Cu_3SbS_4 exhibits VBM and CBM at Γ -point leading to a direct bandgap with a value of 1.0 eV as estimated by the HSE06 functional, which agrees well with both the direct and indirect energy bandgap values determined by experiments.

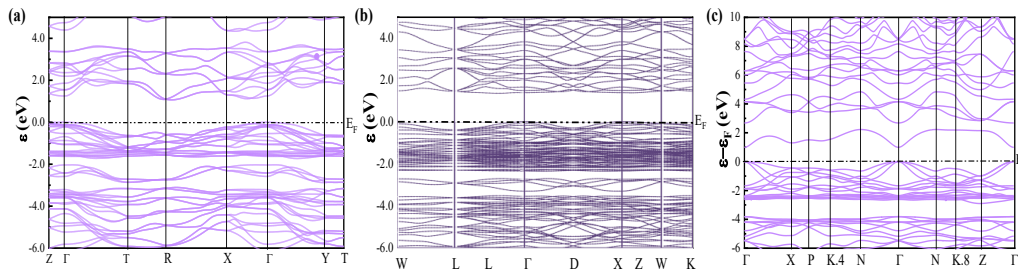


Fig. 2. Band structures of CuSbS_2 (a) and Cu_3SbS_3 (b) crystals calculated with the mBJ functional, and Cu_3SbS_4 (c) calculated with the hybrid HSE06 functional.

Table II. Calculated band gaps of the Cu-Sb-S compounds compared with the literature data.

Chemical compound	Transition type	E_g (eV)	Method	Ref
CuSbS ₂ (Chalcostibite)	Direct	1.4	Exp. (Transmission)	[2]
	Indirect	1.1	Exp. (Absorbance)	[3]
	Indirect	1.6	Calc. (DFT, HSE06)	[3]
	Indirect	1.69	Calc. (DFT, HSE06)	[28]
	Indirect	0.9	Calc. (DFT, PBE)	[28]
	Direct	1.2	Exp. (Reflectance)	[29]
	Indirect	1.0	Exp. (Reflectance)	[29]
	N/A	1.53	Exp. (Absorbance)	[34]
	Direct	1.58	Exp. (Absorbance)	[35]
	Indirect	1.28	Calc. (DFT, mBJ)	[16]
	Indirect	1.72	Calc. (DFT, HSE06)	[17]
	Indirect	0.79	Calc. (DFT, PBE)	[17]
	Indirect	1.16	Calc. (DFT, HSE06)	[18]
	Indirect	0.77	Calc. (DFT, PBE)	[18]
	Indirect	0.885	Calc. (DFT, PBE)	This work
Indirect	1.178	Calc. (DFT, mBJ)	This work	
Cu ₃ SbS ₃ (Skinnerite)	Direct	1.4	Exp. (Absorbance)	[3]
	Direct	1.5	Calc. (DFT, HSE06)	[3]
	Direct	1.85	Exp. (Reflectance)	[29]
	Indirect	1.52	Exp. (Reflectance)	[29]
	Direct	1.46	Exp. (Reflectance)	[30]
	N/A	0.93	Exp. (Absorbance)	[34]
	Direct	1.6	Exp. (Reflectance)	[36]
	Direct	1.87	Exp. (Absorbance)	[37]
	Indirect	1.072	Calc. (DFT, PBE)	This work
	Direct	1.283	Calc. (DFT, mBJ)	This work
Cu ₃ SbS ₄ (Famatinite)	Indirect	1.2	Exp. (Absorbance)	[3]
	Indirect	2.5	Calc. (DFT, HSE06)	[3]
		0.85	Calc. (DFT, HSE06)	[32]
		0.58	Calc. (quasi-particle self-consistent GW)	[17]
	Direct	0.9	Exp. (Absorbance)	[38]
	N/A	1.72	Exp (Absorbance)	[34]
	Direct	0.82	Exp. (Reflectance)	[39]
		0.47	Exp. (Absorbance)	[40]
	Indirect	1.0	Exp. (Absorbance)	[41]
	Direct	0.89	Exp. (Ultraviolet photoelectron spectroscopy)	[42]
	Direct	0.39	Calc. (DFT, HSE06)	[19]
		0.0	Calc. (DFT, PBE)	This work
		0.0	Calc. (DFT, mBJ)	This work
Direct	1.0	Calc. (DFT, HSE06)	This work	

The energetic distributions of the electronic states for CuSbS₂ and Cu₃SbS₃ compounds have been investigated by calculating the density of states with the mBJ potential functional, and for the Cu₃SbS₄ compound by the hybrid HSE06 functional. Fig. 3 shows the atom-projected and orbital-projected density of states (aDOS and oDOS) for Cu-Sb-S compounds in the energy range from -7 to 7 eV. The aDOS contains different energy regions and is contributed by each atom of the crystal system (Fig. 3 a, c, and e), while the oDOS represents the

contribution of different orbital states of the interconnected atoms (Fig. 3 b, d, and f). The fully occupied d orbitals of Sb are not considered in our study. For CuSbS₂, the region [-6.0; -1.7] eV is mainly contributed by Cu and S atoms and slightly by Sb ones. These contributions correspond to Cu-3d and S-3p, and to a lesser extent by Sb-5p/5s, particularly in the region [-2.9; -1.97] eV. The regions [-1.7; 0.0] eV and [1.0; 3.8] eV are mainly contributed by Cu and S with a predominance of Cu-3d orbitals and S-3p orbitals hybridization, and by Sb and S atoms corresponding to mixing of Sb-5p and S-3p orbitals, respectively. The region [4.35; 7.0] eV mainly contains the Cu, Sb, and S atoms contributions, which correspond to Cu-4s, S-3p, and Sb-5p orbitals interactions. For Cu₃SbS₃, four regions can be observed, namely [-6.16; -2.52] eV contributed by Cu, Sb and S atoms (Cu-3d, S-3p and small contribution of Sb-5p/5s), [-2.52; 0.0] eV mainly contributed by Cu atom and very small contribution of S atom (Cu-3d and S-3p), [1.18; 4.0] eV mainly contributed by Sb and S atoms (Sb-5p and S-3p orbitals) and [4.0; 7.0] eV contributed by Cu, Sb and S atoms (Cu-4s, S-3p and Sb-5p orbitals). The DOS of Cu₃SbS₄ compound can be divided into five regions separated by energy gaps. These regions are [-7.32; -4.34] eV, which is contributed by Cu, S and to a lesser extent by Sb (Cu-3d, S-3p, and Sb-5p orbital at higher energy (> -5.98 eV)), [-3.47; -0.56] eV, which is mainly contributed by Cu and to a lesser extent by S (Cu-3d and S-3p orbitals interactions), [0.7; 1.65] eV, which is composed of Cu, Sb and S atoms (Sb-5s and S-3p and small contribution of Cu-3d orbitals), [2.2; 4.03] eV, which is mainly assigned to Sb and a small contribution of S atoms (Sb-5p and S-3p orbitals) and [4.2; 7.0] eV, which is attributed to Cu, Sb and S atoms (Cu-4s, Sb-5p, and S-3p orbitals interactions). It is found that the DOS peaks located at the vicinity of the valence band maximum of CuSbS₂, Cu₃SbS₃, and Cu₃SbS₄ are predominated by a strong Cu-3d and S-3p orbitals hybridization. The conduction band of both CuSbS₂ and Cu₃SbS₃ is mainly contributed by mixing of Sb-5p and S-3p orbital, while the conduction band of Cu₃SbS₄ is dominated by mixing of Sb-5s and S-3p orbitals. As the oxidation state of copper is +I in all the Cu-Sb-S compounds (Cu⁺, 3d¹⁰), the 3d¹⁰ orbitals in the valence band are fully occupied, therefore, a very small contribution of Cu-3d orbital states occurs in the conduction band. The contribution of Sb-5s orbital is very small in the VBM region of CuSbS₂ and Cu₃SbS₃, thus the Sb 5s electrons have weak interaction with S-3p and become chemically inert as lone-pair electrons. As it was observed in PbS [43], the crystal systems in which CuSbS₂, and Cu₃SbS₃ crystallize, namely orthorhombic and monoclinic, are dictated by this electron lone pair, which necessitates a distortion of the crystal lattice to be energetically stable. Despite having an inert effect on chemical bonds, this electron lone pair has a stereochemical effect on the crystal structure and is only involved in van der Waals interactions. By contrast, in the case of Cu₃SbS₄, (Cu^ISb^VS^{-II}) there is no pure Sb-5s orbital accommodating electrons, and the atoms are connected via covalent

bonds to form Chalcopyrite tetrahedral structure. Therefore, the Cu-Sb-S compounds offer various bonding properties that deserve investigation through the topological analysis of the electron density.

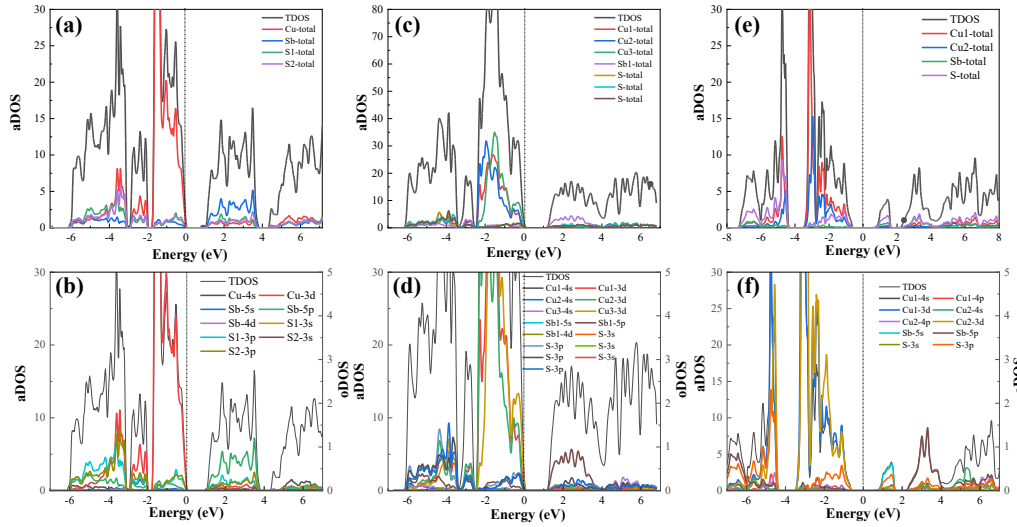


Fig. 3. Atom-projected density of states (aDOS) and orbital-projected density of states (oDOS) for CuSbS₂ (a, and b) and Cu₃SbS₃ (c, and d) calculated with the mBJ functional, and Cu₃SbS₄ (e, and f) calculated with the HSE06 functional.

3.3. Electron density topological properties of the Cu-Sb-S system compounds

Since the knowledge on structure-property relationship is still limited, investigating quantum-mechanical atomic and molecular interactions in solid crystals is relevant in view of material design for the targeted application. In this context, the investigation of electron density in real space within solids has been studied by the quantum theory of atoms in molecules (QTAIM) using Critic2 program. The calculated electron density Laplacians in the (-110) plane of CuSbS₂, Cu₃SbS₃, and Cu₃SbS₄ are depicted in Fig. 4a, Fig. 4b, and Fig. 4c, respectively. The symbols b, r, and c represent bond, ring, and cage critical points, respectively, as described in the QTAIM theory. Bond length, bond angle, electron density (ρ_{BCP}), electron density Laplacian ($\nabla^2\rho_{BCP}$), ellipticity, and local electron kinetic (V_{BCP}), potential (G_{BCP}), and total energy (H_{BCP}) densities at bond critical points (BCP) extracted from Critic2 program outputs are gathered in Table S1. The relation between electron density Laplacian, kinetic energy G_{BCP} , and potential energy V_{BCP} densities at BCP is given by:

$$\frac{\hbar^2}{4m} \nabla^2 \rho_{BCP} = 2G_{BCP} + V_{BCP}, \quad (10)$$

and the variation of bond degree ($BD = H_{BCP}/\rho_{BCP}$) versus $|V_{BCP}|/G_{BCP}$ ratio can be used to distinguish bonding types [44]. Figure 4d shows these characteristics for CuSbS₂, Cu₃SbS₃, and Cu₃SbS₄. A linear evolution is observed with a correlation coefficient R^2 of 0.904, 0.993, and 0.867, respectively. Three and seventeen different Cu-S bonds can be evidenced in CuSbS₂ and Cu₃SbS₃, respectively (see Table S1). The longest Cu-S bond in

each Cu-Sb-S structure is distinguished with an asterisk sign (*) in Figure 4d. Although the electron density Laplacian (Figure 4a-c) for Cu-S bonds differs from one structure to another, the kinetic energies per electron at the bond critical point ($G_{\text{BCP}}/\rho_{\text{BCP}}$), which are related to the polarizability of the charge distribution [44], are almost the same (comprised between 0.82 and 0.87, see Table S1). The best concordance is observed between CuSbS_2 and Cu_3SbS_3 (Fig. 4d). Moreover, the local energy densities for CuSbS_2 and Cu_3SbS_3 are all very close to one another on the graph. All these results suggest that the Cu-S bonds in CuSbS_2 , Cu_3SbS_3 , and Cu_3SbS_4 have close bonding characteristics, though not strictly the same due to the difference in atoms environment. In agreement with Ref. [44], for similar $G_{\text{BCP}}/\rho_{\text{BCP}}$ the interatomic distances increase with the absolute value of the bond degree. This is exemplified for the Cu-S bonds in Fig. 4e, though this holds for the Sb-S bonds, too. Espinosa et al. classified the bonds into three categories based on the $|V_{\text{BCP}}|/G_{\text{BCP}}$ ratio and bond degree (BD) $H_{\text{BCP}}/\rho_{\text{BCP}}$ [45]: Pure closed-shell (CS) including ionic bond, hydrogen bond, and van der Waals interactions ($|V_{\text{BCP}}|/G_{\text{BCP}} < 1$), pure shared-shell (SS) including covalent and polar bonds ($|V_{\text{BCP}}|/G_{\text{BCP}} > 2$), and bonds belonging to the transit region with positive Laplacian and negative total energy density ($1 < |V_{\text{BCP}}|/G_{\text{BCP}} < 2$). It has been found that the Cu-S and Sb-S bonds for Cu-Sb-S structures lie in the transit zone, between the typical ionic and covalent bonds. The Sb-Sb and Cu-Cu bonds for CuSbS_2 and Cu_3SbS_3 , respectively, lie close to the point ($|V_{\text{BCP}}|/G_{\text{BCP}}=1$, $H_{\text{BCP}}/\rho_{\text{BCP}}=0$), which correspond to non-localized interactions. The accumulation of electron density at BCP is generally increased along bond path as the bond length decreases. This means large overlapping of electron clouds and increased refractive index of the materials. The optical properties of the semiconductor materials under incident photons depend on the electron transition from valence band maximum to empty conduction band minimum, attributed in the compounds of interest to mixing of Cu-3d/S-3p and Sb-5p or Sb-5s/S-3p, respectively. The Sb-S with a large bond degree revealed a high absorption coefficient ($> 10^4 \text{ cm}^{-1}$) of Cu-Sb-S materials near the Fermi level. These results should lead to a lower bandgap of CuSbS_2 compared to that of Cu_3SbS_4 . However, the presence of empty Sb-5s orbital in the conduction band causes a Sb-5s/S-3p hybridization in the case of Cu_3SbS_4 , which confers it a lower bandgap than expected, leading to a reversed bandgap order between CuSbS_2 and Cu_3SbS_4 as shown in Fig. 2 and Fig. 3.

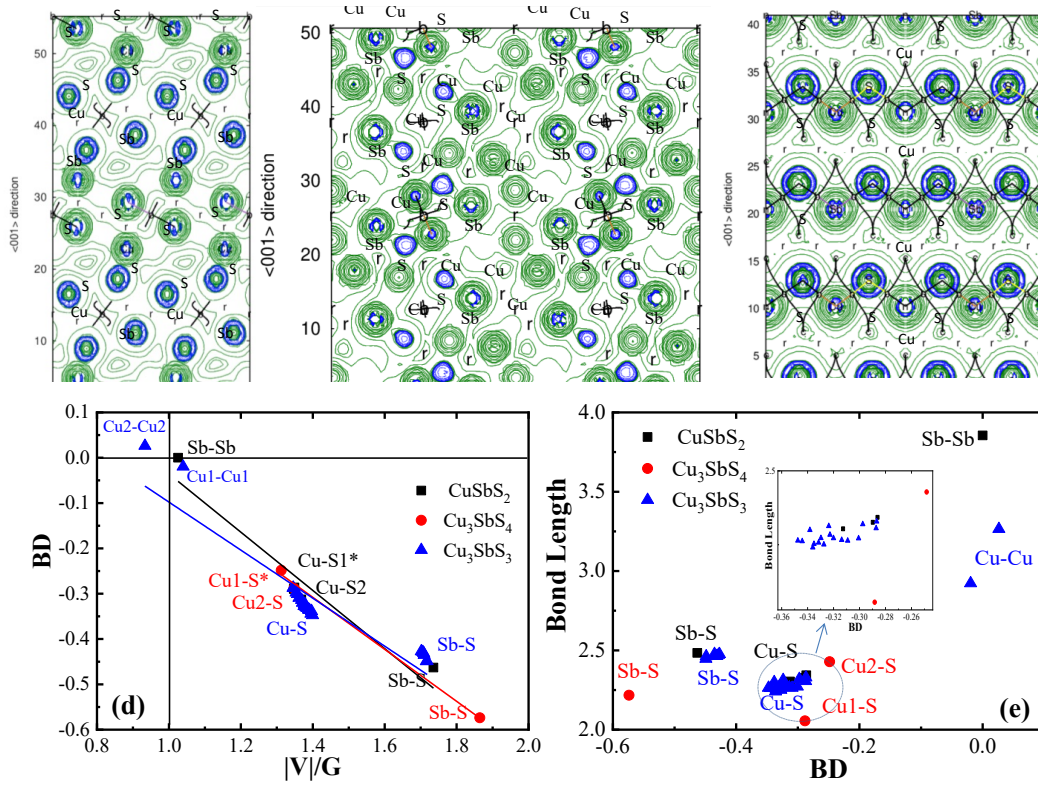


Fig. 4. Electron density Laplacian of CuSbS₂ (a), Cu₃SbS₃ (b) and Cu₃SbS₄ (c). (d) Bond degree vs. $|V_{BCP}|/G_{BCP}$. (*) represents the longest bond length for each pairwise. (e) Relation between bond length and bond degree at BCPs for Cu-Sb-S system compounds.

3.4 Optical properties of Cu-Sb-S system compounds

Further, the valence band maximum (VBM) of Cu-Sb-S structures is mainly due to the mixing of Cu-3d and S-3p, which can stabilize the holes and provides high mobility Cu/S framework paths. The optical properties of CuSbS₂ and Cu₃SbS₃ have been calculated using the mBJ potential functional, while those of Cu₃SbS₄ have been calculated using the HSE06 functional one. The refractive index, extinction coefficient, absorption coefficient, and reflectivity have been determined by utilizing the calculated dielectric function as described in the computational section. For Cu₃SbS₄ with a tetragonal structure, the optical functions are analysed along with two directions, namely xx and zz, while for CuSbS₂ and Cu₃SbS₃ with orthorhombic and monoclinic structures the optical properties are analysed according to the three diagonal components xx, yy, and zz. The dielectric function $\epsilon(\omega)$ characterizes the collective excitations close to the Fermi-level and depends strongly on the band structure [46]. The calculated dielectric functions for CuSbS₂, Cu₃SbS₃, and Cu₃SbS₄ are depicted in Fig. 5, the real parts $\epsilon_1(\omega)$ of which being shown in Fig. 5a, 5c and 5e and the imaginary parts $\epsilon_2(\omega)$ of which being shown in Fig. 5b, 5d and 5f. The maximum peak values of $\epsilon_1(\omega)$ for CuSbS₂ (Fig. 5a), Cu₃SbS₃ (Fig. 5c), and Cu₃SbS₄ (Fig. 5e) are fair agreement with those reported in literature (Ref [16] for CuSbS₂ and Ref [19] for Cu₃SbS₄).

$\epsilon_1(\omega)$ becomes negative above a certain photon energy: about 6 eV for the CuSbS₂ and Cu₃SbS₃ compounds, and about 8 eV for Cu₃SbS₄. This indicates that the Cu-Sb-S materials have a metallic character above these photon energy thresholds [16]. At zero frequency limit ($\omega = 0$), $\epsilon_1(\omega)$ gives the static dielectric permittivity. Higher static dielectric permittivity values have been obtained for Cu₃SbS₄ indicating higher polarizability for this compound. This result agrees with the G_{BCP}/ρ_{BCP} values (Table S1) since lower G_{BCP}/ρ_{BCP} corresponds to higher polarizability [44]. According to the Penn model [47] $\epsilon_1(0)$ is defined as $\epsilon_1(0) \approx 1 + (\hbar\omega/E_g)^2$, where $\hbar\omega$ is the plasma energy. Hence, the band gap of the Cu-Sb-S materials should increase when going from Cu₃SbS₄ to CuSbS₂ and to Cu₃SbS₃. This is supported by our band gap calculations (see section 3.2). The maximum peak values of $\epsilon_2(\omega)$ for the xx, yy and zz components are: 12.05, 13.117, and 14.061 at 2.19, 2.325, and 2.326 eV for CuSbS₂ (Figure 5b); 9.79, 13.483, and 13.257 at 2.918, 3.012, and 3.012 eV for Cu₃SbS₃ (Figure 5d); 6.815, 6.815 and 7.974 at 7.855, 7.855, and 7.797 eV for Cu₃SbS₄ (Fig. 5f). Along the series CuSbS₂, Cu₃SbS₃, Cu₃SbS₄ the decreasing tendency of $\epsilon_2(\omega)$ values and the shift of the peak maximum towards higher incident energies indicate a decrease of the ability of the Cu-Sb-S compounds to absorb light. Thus, CuSbS₂ compound has the highest ability to absorb the incident light although it has indirect bandgap [33]. Compared with theoretical data reported in the literature [16, 19] for CuSbS₂ and Cu₃SbS₄, the following comments can be made. For CuSbS₂ the maximum values of $\epsilon_2(\omega)$ are in fair agreement with ours, the peak being slightly shifted towards lower photon energies in our case. The agreement is worse for Cu₃SbS₄ as the peak reported by Li et al. [19] is significantly shifted toward lower photon energies. This might be explained by their band gap for Cu₃SbS₄ that they found much smaller than ourselves. The difference in the energy gaps can also explain the differences observed in the absorption results between our results and those of Ramasamy et al. [3] for Cu₃SbS₄. As they mentioned in their article, the calculated gap is highly overestimated. By contrast for Cu₃SbS₃, both the energy gap and the absorption spectrum calculated in [3] are close to ours.

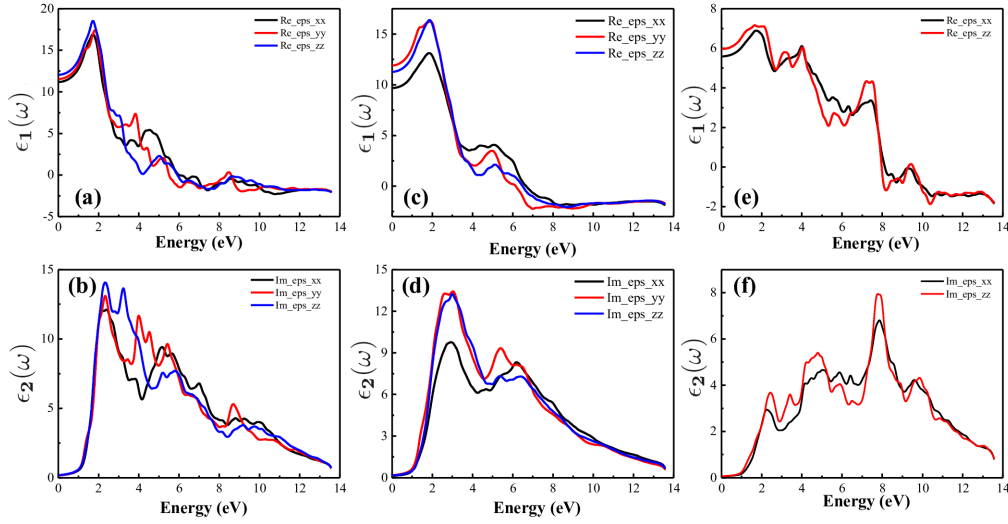


Fig. 5. Real and imaginary dielectric functions of Cu-Sb-S materials: (a, and b) CuSbS₂; (c, and d) Cu₃SbS₃; (e, and f) Cu₃SbS₄.

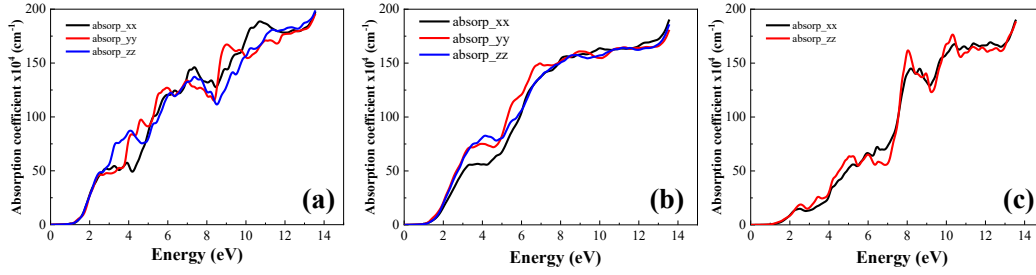


Fig. 6. Absorption coefficient of Cu-Sb-S materials: (a) CuSbS₂, (b) Cu₃SbS₃ and (c) Cu₃SbS₄.

The absorption coefficient spectra $\alpha(\omega)$ of CuSbS₂, Cu₃SbS₃, and Cu₃SbS₄ are plotted in Fig. 6a, 6b, and 6c, respectively. As the photon energy increases the absorption coefficient of these materials increases, showing successive peaks of increasing intensity, which is a typical feature of semiconductors. These absorption peaks correspond to various electronic transitions from the valence band to the conduction one. The band gaps calculated along the xx, yy and zz directions are 1.182, 1.089, and 1.161 eV for CuSbS₂, 1.286, 1.299 and 1.298 eV for Cu₃SbS₃, and 1.01, 1.01 and 1.03 eV for Cu₃SbS₄, respectively. In the visible light region, at 1.59 eV (780 nm), the absorption coefficient values along the xx direction are 8.07×10^4 , 5.78×10^4 and 3.01×10^4 , cm⁻¹ for CuSbS₂, Cu₃SbS₃, and Cu₃SbS₄, respectively, while being 54.69×10^4 , 55.76×10^4 and 15.67×10^4 cm⁻¹ at 3.26 eV (380 nm).

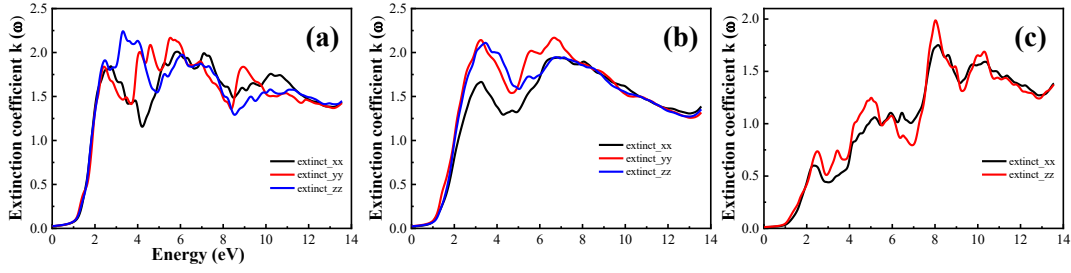


Fig. 7. Extinction coefficient of Cu-Sb-S materials: (a) CuSbS_2 , (b) Cu_3SbS_3 and (c) Cu_3SbS_4 .

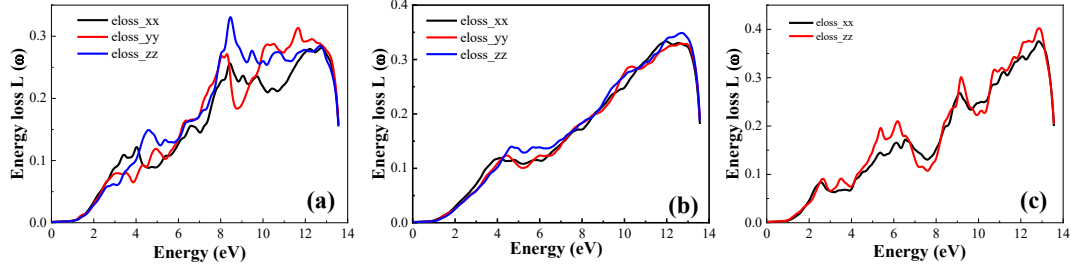


Fig. 8. Energy loss of Cu-Sb-S materials: (a) CuSbS_2 , (b) Cu_3SbS_3 and (c) Cu_3SbS_4 .

Fig. 7 shows the variation of the extinction coefficient $k(\omega)$ with photon energy for CuSbS_2 , Cu_3SbS_3 , and Cu_3SbS_4 . The maximum values of the extinction coefficient along the xx, yy and zz directions are: 2.022, 2.169, and 2.245 at 5.834, 5.528, and 3.315 eV for CuSbS_2 ; 1.948, 2.175, and 2.107 at 6.508, 6.680, and 3.433 eV for Cu_3SbS_3 ; and 1.75, 1.75, and 1.98 at 8.02, 8.02 and 8.12 eV for Cu_3SbS_4 . These results indicate high efficiency of the Cu-Sb-S system compounds for photovoltaic applications due to absorption of the most intense part of the sun radiation. The calculated energy loss $L(\omega)$ for CuSbS_2 , Cu_3SbS_3 , and Cu_3SbS_4 are shown in Fig. 8a, 8b, and 8c, respectively. The highest peak values along the xx, yy and zz directions are: 0.201, 0.313, and 0.332 at 12.769, 11.656, and 8.471 eV for CuSbS_2 ; 0.334, 0.329, and 0.348 at 12.825, 12.568, and 12.710 eV for Cu_3SbS_3 ; 0.375, 0.375, and 0.403 at 12.825, 12.825, and 12.865 eV for Cu_3SbS_4 . These maximum peaks are associated to bulk plasmon, which gives information about strain in solid materials [48]. Thus, Cu_3SbS_3 and Cu_3SbS_4 compounds offer better relative stability for photovoltaic applications compared to CuSbS_2 .

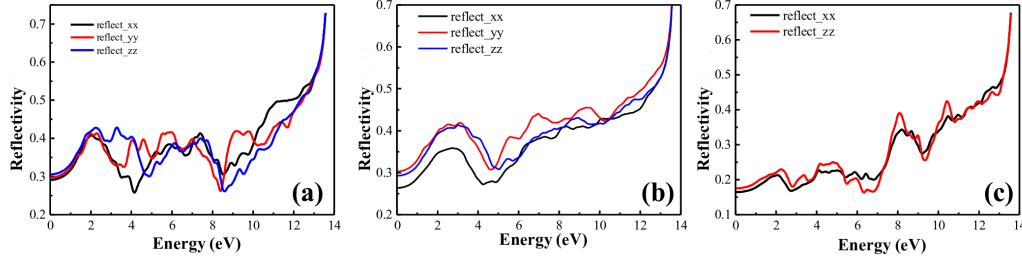


Fig. 9. Reflectivity of Cu-Sb-S materials: (a) CuSbS₂, (b) Cu₃SbS₃ and (c) Cu₃SbS₄.

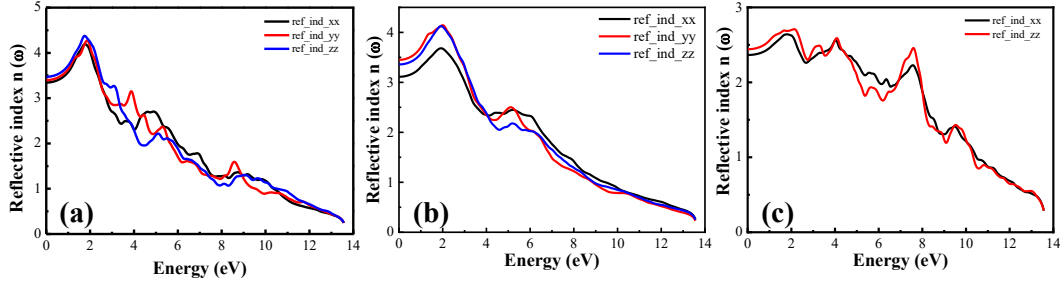


Fig. 10. Refractive index of Cu-Sb-S materials: (a) CuSbS₂, (b) Cu₃SbS₃ and (c) Cu₃SbS₄.

Fig. 9 shows the reflectivity $R(\omega)$ of CuSbS₂, Cu₃SbS₃, and Cu₃SbS₄ with respect to photon energy. Due to the presence of collective plasma resonance [49], a sudden reduction is observed at 4.13 and 8.54 eV for CuSbS₂, 4.6 eV for Cu₃SbS₃ and 2.679, 6.869, and 9.271 eV for Cu₃SbS₄. The refractive index values $n(\omega)$ of CuSbS₂, Cu₃SbS₃ and Cu₃SbS₄ are depicted in Fig. 10a, 10b, and 10c, respectively. At zero frequency limit ($\omega = 0$), the static refractive indices $n(0)$ are $n_{xx} = 3.326$, $n_{yy} = 3.403$, and $n_{zz} = 3.479$ for CuSbS₂, $n_{xx} = 3.108$, $n_{yy} = 3.452$, and $n_{zz} = 3.357$ for Cu₃SbS₃, $n_{xx} = n_{yy} = 2.258$, and $n_{zz} = 2.449$ for Cu₃SbS₄. The maximum values of $n(\omega)$ along the xx, yy and zz components are: 4.189, 4.269, and 4.381 at 1.766, 1.861, and 1.748 eV for CuSbS₂; 3.684, 4.144, and 4.120 at 1.923, 1.998, and 1.899 eV for Cu₃SbS₃; 1.762, 1.762 and 2.116 at 2.645, 2.645, and 2.714 eV for Cu₃SbS₄. According to these values, since the speed of light passing through the materials depends on their refractive index, the speed of light should decrease along the sequence Cu₃SbS₃, Cu₃SbS₄ and CuSbS₂.

4. Conclusions

The electronic, QTAIM topological, and optical characteristics of CuSbS₂, Cu₃SbS₃, and Cu₃SbS₄ compounds have been theoretically explored by utilizing WIEN2k package to provide fundamental insights and understand their relevance applicability for photovoltaics. The CuSbS₂, Cu₃SbS₃, and Cu₃SbS₄ exhibit bandgap energy of $E_g = 1.178$, 1.283, and 1.0 eV, respectively, which are mainly attributed to a strong Cu-3d and S-3p orbitals hybridization in VBM and Sb-5p/Sb-5s orbitals and S-3p orbital mixing in CBM. The three Cu-Sb-S compounds exhibit high absorption coefficient ($> 10^4 \text{ cm}^{-1}$) with relative stability in visible light region. The electron density

topological studies revealed that the Cu-S bonds in CuSbS_2 , Cu_3SbS_3 , and Cu_3SbS_4 have close bonding characteristics, though not strictly the same due to the difference in atoms environment. In addition, non-localized interactions prevail in Sb-Sb and Cu-Cu bonds in CuSbS_2 and Cu_3SbS_3 , respectively. This study brings new results on electronic and optical properties of CuSbS_2 , Cu_3SbS_3 , and Cu_3SbS_4 as well as original ones on their bonding characteristics. In the electronic and optical properties investigations already published, though the authors used HSE06 functional, the band gap was either under- or overestimated in comparison with experimental data, which could impact negatively the optical properties. Our work evidences that the HSE06 functional yields good electronic gaps and properties, provided that well converged technical parameters (plane-wave cutoff energy and k-point grid) are employed. The setting of these parameters is a limiting feature for DFT investigations. In future work this study will be extended by combining macroscopic properties with microscopic ones into a quantitative structure-property relationship model that will allow for the design of efficient materials.

Acknowledgments

The authors acknowledge the Egyptian-French cooperation program provided by the French Institute and the Science and Technology Fund (STDF-IFE) in Egypt, Grant No. 31127 for the financial support. This work was granted access to the HPC resources of the Centre Informatique National de l'Enseignement Supérieur (CINES), Montpellier, France under allocation A0090806881 made by the Grand Equipement National de Calcul Intensif (GENCI). It was also granted access to the HPC resources of Aix-Marseille University financed by the project Equip@Meso (ANR-10-EQPX-29-01) of the program "Investissements d'Avenir" supervised by the Agence Nationale de la Recherche.

Supplementary data

Fig. S1: Band structure of CuSbS_2 (a), Cu_3SbS_4 (b) and Cu_3SbS_3 (c) calculated with GGA-PBE functional. Fig. S2: Band structure of Cu_3SbS_4 calculated with mBJ functional. Table S1: Electron density topological properties of Cu-Sb-S materials.

Conflict of interest: The authors declare that they have no conflict of interest.

References

- [1] Y.-Y. Sun, M. L. Agiorgousis, P. Zhang, S. Zhang, Chalcogenide Perovskites for Photovoltaics, *Nano Lett.* 15, 581-585 (2015).

- [2] B. Yang, L. Wang, J. Han, Y. Zhou, H. Song, S. Chen, J. Zhong, L. Lv, D. Niu, J. Tang, CuSbS₂ as a Promising Earth-Abundant Photovoltaic Absorber Material: A Combined Theoretical and Experimental Study, *Chem. Mater.* 26, 3135-3143 (2014).
- [3] K. Ramasamy, H. Sims, W. H. Butler, A. Gupta, Selective Nanocrystal Synthesis and Calculated Electronic Structure of All Four Phases of Copper–Antimony–Sulfide, *Chem. Mater.* 26, 2891-2899 (2014).
- [4] T. K. Todorov, J. Tang, S. Bag, O. Gunawan, T. Gokmen, Y. Zhu, D. B. Mitzi, Beyond 11% Efficiency: Characteristics of State-of-the-Art Cu₂ZnSn(S,Se)₄ Solar Cells, *Adv. Energy Mater.* 3, 34–38 (2013).
- [5] F. Mohamadkhani, M. Heidariramsheh, S. Javadpour, E. Ghavaminiya, S. M. Mahdavi, N. Taghavinia, Sb₂S₃ and Cu₃SbS₄ nanocrystals as inorganic hole transporting materials in perovskite solar cells. *Solar Energy* 223, 106-112 (2021).
- [6] L. Lin, G. Chen, L. Yao, Z. Huang, H. Li, F. Wu, W. Lin, Y. Mao, Z. Huang, Antimony loss and composition-dependent phase evolution of CuSbS₂ absorber using oxides nanoparticles ink. *Mater. Sci. Semicond. Process.* 133, 105944 (2021).
- [7] N. Chlibi, J. P. B. Silva, E. M. F. Vieira, L. M. Goncalves, J. A. Moreira, A. Chahboun, H. Dahman, M. Pereira, M. J. M. Gomes, E. L. Mir, Touch sensor and photovoltaic characteristics of CuSbS₂ thin films. *Ceramics Int.* 47, 22594-22603 (2021).
- [8] S. A. Zaki, M. I. Abd-Elrahman, A. A. Abu-Sehly, N. M. Shaalan, M. M. Hafiz, Solar cell fabrication from semiconducting Cu₃SbS₃ on n-Si: Parameters evolution. *Mater. Sci. Semicond. Process.* 115, 105123 (2020).
- [9] G. K. Gupta, A. Dixit, Simulation studies on photovoltaic response of ultrathin CuSb(S/Se)₂ ternary compound semiconductors absorber-based single junction solar cells. *Int. J. Energy Res.* 44, 3724-3736 (2020).
- [10] B. H. Kumar, S. Shaji, M. C. S. Kumar, Effect of substrate temperature on properties of co-evaporated copper antimony sulfide thin films. *Thin Solid Films* 697, 137838 (2020).
- [11] L. Wan, X. Guo, Y. Fang, X. Mao, H. Guo, J. Xu, R. Zhou, Spray pyrolysis deposited CuSbS₂ absorber layers for thin-film solar cells. *J. Mater. Sci.* 30, 21485-21494 (2019).
- [12] S. Banu, Y. Cho, K. Kim, S. K. Ahn, J. Gwak, A. Cho, Phase transition behavior and defect analysis of CuSbS₂ thin films for photovoltaic application prepared by hybrid inks. *Solar Energy* 188, 1209-1220 (2019).

- [13] G. Han, J. W.; Lee, J. Kim, Fabrication and Characterization of Cu_3SbS_4 Solar Cell with Cd-free Buffer. *J. Korean Phys. Soc.* 73, 1794-1798 (2018).
- [14] L. Yu, R. S. Kokenyesi, D. A. Keszler, A. Zunger, Inverse Design of High Absorption Thin-Film Photovoltaic Materials, *Adv. Energy Mater.* 3, 43-48 (2013).
- [15] R. F. W. Bader, *Atoms in Molecules*, Clarendon Press: Oxford, UK, (1990).
- [16] A. Gassoumi, H.-E M. Musa Saad, S. Alfaify, T. B. Nasr, N. Bouariss, The investigation of crystal structure, elastic and optoelectronic properties of CuSbS_2 and CuBiS_2 compounds for photovoltaic applications, *J. Alloys Compd.* 725, 181-189 (2017).
- [17] M. Kumar, C. Persson, CuSbS_2 and CuBiS_2 as potential absorber materials for thin-film solar cells, *J. Renewable Sustainable Energy* 5, 031616 (2013).
- [18] T. Maeda, T. Wada, First-principles study of electronic structure of CuSbS_2 and CuSbSe_2 photovoltaic semiconductors, *Thin solid film* 582, 401-407 (2015).
- [19] J. Li, X. Han, J. Li, Y. Zhao, C. Fan, Structural, electronic and optical properties of famatinite and enargite Cu_3SbS_4 under pressure: A theoretical investigation. *Phys. Status Solidi (b)* 254, 1600608 (2016).
- [20] P. Blaha, K. Schwarz, G. K. H. Madsen, D. Kvasnicka, J. Luitz, WIEN2k, an augmented plane wave + local orbitals program for calculating crystal properties Karlheinz Schwarz, Techn. Universität Wien, Austria, (2001).
- [21] J. P. Perdew, K. Burke, M. Ernzerhof, Generalized Gradient Approximation Made Simple, *Phys. Rev. Lett.* 77, 3865-3868 (1996).
- [22] D. Koller, F. Tran, P. Blaha, Merits and limits of the modified Becke-Johnson exchange potential, *Phys. Rev. B* 83, 195134 (2011).
- [23] W. Khan, A. H. Reshak, Optoelectronic and thermoelectric properties of KAuX_5 ($X = \text{S}, \text{Se}$): a first principles study, *J. Mater. Sci.* 49, 1179-1192 (2014).
- [24] F. Tran, P. Blaha, Accurate Band Gaps of Semiconductors and Insulators with a Semilocal Exchange-Correlation Potential, *Phys. Rev. Lett.* 102, 226401 (2009).
- [25] J. Heyd, G. E. Scuseria, M. Ernzerhof, Hybrid functionals based on a screened Coulomb potential, *J. Chem. Phys.* 118, 8207-8215 (2003).
- [26] C. Ambrosch-Draxl, J. Sofo, Linear optical properties of solids within the full-potential linearized augmented planewave method. *Comput. Phys. Commun.* 175, 1-14 (2006).

- [27] A. Otero-de-la-Roza, E.R. Johnson, V. Luaña, Critic2: A program for real-space analysis of quantum chemical interactions in solids. *Comput. Phys. Commun.* 185, 1007-1018 (2014).
- [28] J. T. R. Dufton, A. Walsh, P. M. Panchmatia, L. M. Peter, D. Colombara, M. S. Islam, Structural and electronic properties of CuSbS₂ and CuBiS₂: potential absorber materials for thin-film solar cells, *Phys. Chem. Chem. Phys.* 14, 7229-7233 (2012).
- [29] D. Xu, S. Shen, Y. Zhang, H. Gu, Q. Wang, Selective Synthesis of Ternary Copper–Antimony Sulfide Nanocrystals, *Inorg. Chem.* 52, 12958-12962 (2013).
- [30] K. Nefzi, A. Rabhi, M. Kanzari, Investigation of physical properties and impedance spectroscopy study of Cu₃SbS₃ thin films, *J Mater Sci: Mater. Electron.* 27, 1888-1896 (2016).
- [31] J. Embden, Y. Tachibana, Synthesis and characterisation of famatinitite copper antimony sulfide nanocrystals, *J. Mater. Chem.* 22, 11466-11469 (2012).
- [32] K. Chen, C. Di Paola, B. Du, R. Zhang, S. Laricchia, N. Bonini, C. Weber, I. Abrahams, H. Yan, M. Reece, Enhanced thermoelectric performance of Sn-doped Cu₃SbS₄, *J. Mater. Chem. C* 6, 8546-8552 (2018).
- [33] P. Jiang, P. Boulet, M.-C. Record, A DFT study of the electronic, optical and topological properties of free and biaxially strained CuIn_{1-x}Al_xSe₂, *J. Mater. Chem. C* 7, 5803-5815 (2019).
- [34] S. Ikeda, S. Sogawa, Y. Tokai, W. Septina, T. Harada, M. Matsumura, Selective production of CuSbS₂, Cu₃SbS₃, and Cu₃SbS₄ nanoparticles using a hot injection protocol, *RSC Adv.* 4, 40969-40972 (2014).
- [35] M. E. Edley, B. Opananont, J. Conley, H. Tran, S. Y. Smolin, S. Li, A. D. Dillon, A. T. Fafarman, J. B. Baxter, Solution processed CuSbS₂ films for solar cell applications, *Thin Solid Films* 646, 180-189 (2018).
- [36] A. Hussain, R. Ahmed, N. Ali, A. Shaari, J.-T. Luo, Y. Q. Fu, Characterization of Cu₃SbS₃ thin films grown by thermally diffusing Cu₂S and Sb₂S₃ layers, *Surf. Coat. Technol.* 319, 294-300 (2017).
- [37] X. Qiu, S. Ji, C. Chen, G. Liu, C. Ye, Synthesis, characterization, and surface-enhanced Raman scattering of near infrared absorbing Cu₃SbS₃ nanocrystals, *Cryst. Eng. comm.* 15, 10431-10434 (2013).
- [38] G. H. Albuquerque, K. Kim, J. Lopez, A. Devaraj, S. Manandhar, Y. Liu, J. Guo, C. Chang, G. Herman, Multimodal characterization of solution-processed Cu₃SbS₄ absorbers for thin film solar cells, *J. Mater. Chem. A* 6, 8682-8692 (2018).
- [39] U. Chalapathi, B. Poornaprakash, S.-H. Park, Growth and properties of Cu₃SbS₄ thin films prepared by a two-stage process for solar cell applications, *Ceram. Int.* 43, 5229-5235 (2017).
- [40] O. Madelung, Semiconductors: Data Handbook; Springer-Verlag: New York, (2000).

- [41] J. Embden, K. Latham, N. W. Duffy, Y. Tachibana, Near- infrared Absorbing $\text{Cu}_{12}\text{Sb}_4\text{S}_{13}$ and Cu_3SbS_4 Nanocrystals: Synthesis, Characterization, and Photoelectrochemistry. *J. Am. Chem. Soc.* 135, 11562-11571 (2013).
- [42] Q. Zeng, Y. Di, C. Huang, K. Sun, Y. Zhao, H. Xie, D. Niu, L. Jiang, X. Hao, Y. Lai, F. Liu, Famatinite Cu_3SbS_4 nanocrystals as hole transporting material for efficient perovskite solar cells. *J. Mater. Chem. C* 6, 7989-7993 (2018).
- [43] A. Walsh, G. W. Watson, The origin of the stereochemically active Pb(II) lone pair: DFT calculations on PbO and PbS. *J. Solid State Chem.* 178, 1422-1428 (2005).
- [44] H. Yang, P. Boulet, M.-C. Record, A rapid method for analyzing the chemical bond from energy densities calculations at the bond critical point. *Comput. Theor. Chem.* 1178, 112784 (2020).
- [45] E. Espinosa, I. Alkorta, J. Elguero, E. Molins, From weak to strong interactions: A comprehensive analysis of the topological and energetic properties of the electron density distribution involving X-H...F-Y systems. *J. Chem. Phys.* 117, 5529-5542 (2002).
- [46] B. Amin, R. Khenata, A. Bouhemadou, I. Ahmad, M. Maqbool, Opto-electronic response of spinels MgAl_2O_4 and MgGa_2O_4 through modified Becke-Johnson exchange potential. *Physica B* 407, (2012) 2588-2592 (2002).
- [47] D. R. Penn, Wave-Number-Dependent Dielectric Function of Semiconductors. *Phys. Rev.* 128, 2093-2097 (1962).
- [48] J. Palisaitis, C.-L. Hsiao, M. Junaid, J. Birch, L. Hultman, P. O. A. Persson, Effect of strain on low-loss electron energy loss spectra of group-III nitrides. *Phys. Rev. B* 84, 245301 (2011).
- [49] G. Murtazaa, S. K. Guptab, T. Seddikc, R. Khenatac, Z. A. Alahmedd, R. Ahmede, H. Khachaif, P. K. Jhag, S. Bin Omran, Structural, electronic, optical and thermodynamic properties of cubic REGa_3 (RE = Sc or Lu) compounds: Ab initio study. *J. Alloy Compd.* 597, 36-44, (2014).